# *Numerical exploration of turbulent air natural-convection in a differentially heated square cavity at $Ra = 5.33 \times 10^9$*

**Zheng Zhang, Wei Chen, Zuojin Zhu & Yinglin Li**

**Heat and Mass Transfer**
Wärme- und Stoffübertragung

ISSN 0947-7411
Volume 50
Number 12

Heat Mass Transfer (2014) 50:1737-1749
DOI 10.1007/s00231-014-1339-8

Heat Mass Transfer (2014) 50:1737–1749
DOI 10.1007/s00231-014-1339-8

ORIGINAL

# Numerical exploration of turbulent air natural-convection in a differentially heated square cavity at Ra = 5.33 × 10^9

**Zheng Zhang · Wei Chen · Zuojin Zhu · Yinglin Li**

Received: 7 March 2012 / Accepted: 20 March 2014 / Published online: 11 June 2014


**Abstract** The turbulent air natural-convection in a differentially heated square cavity is certainly a benchmark problem in thermo-hydrodynamics. Using large eddy simulation (LES), the natural convection at a Rayleigh number of $5.33 \times 10^9$ is numerically explored, in which a sub-grid scale model constructed by non-dimensional analysis on the basis of the swirling-strength and the harmonically-averaged grid interval is utilized. A factor of swirling strength intermittency (FSI), which is defined by the ratio of the swirling strength to the magnitude of the complex eigenvalue of the filtered velocity gradient tensor, is used instead of the near-wall length scale decaying factor in the description of the near-wall sub-grid viscosity. The cavity with the height-width-depth ratio of 1:1:2 is partitioned by a non-uniform staggered grid, whose resolution is obtained by the grid number of $100 \times 100 \times 120$ . It was found that to some extent the LES results agree well with the existing experimental data, suggesting that the swirling-strength based sub-grid scale model used in the LES is of potential. Subjected the influences of the loop wall jet and the assigned temperature in the horizontal walls, as can be seen from the *t-z* averaged FSI distribution in the square section, the heterogeneity of the averaged FSI in the near wall regions is more evident, but in the core region of the square cavity, this heterogeneity decreases and the natural convection tends to become relatively homogeneous. The turbulent natural convection at Rayleigh number $5.33 \times 10^9$ certainly has its own geometry-dependent intermittency of turbulence.

Z. Zhang · W. Chen · Z. Zhu (✉) · Y. Li
Faculty of Engineering Science, University of Science and Technology of China, Hefei 230026, People's Republic of China
e-mail: zuojin@ustc.edu.cn
URL: http://staff.ustc.edu.cn/~zuojin

## List of symbols

| | |
|---|---|
| $\mathbf{A} = \nabla \mathbf{u}$ | Matrix for velocity gradient tensor |
| $A_m, B_m$ | $m = 1, 2$, Scheme coefficients |
| $C_\mu$=0.09 | Coefficient to define SGS viscosity $\nu_s$ |
| $f_I$ | Defined by Eq. (2) |
| $H$ | Height of square cavity |
| $Nu_x$, $Nu_y$ | *t-z* averaged Nusselt numbers |
| $\overline{Nu}$ | Nusselt number based on empirical correlation |
| $p$ | Normalized pressure |
| Pr | Prandtl number |
| $\mathbf{R}$ | A force depending on viscosity gradient |
| $Ra$ | Rayleigh number |
| Re | Reynolds number |
| $T$ | Temperature (K) |
| $\mathbf{u}$ | Normalized velocity vector |
| $u_\tau$ | Friction velocity (m/s) |
| $u, v, w$ | Normalized velocity components |
| $W_0 = \sqrt{g\beta_T H \Delta T}$ | Velocity scale (m/s) |
| $x, y, z$ | Cartesian coordinates |

## Greek symbols

| | |
|---|---|
| $\delta$ | The harmonic average of grid intervals (m) |
| $\beta_T$ | Thermal expansion coefficient of fluid (1/K) |
| $\kappa$ | Thermal diffusivity of fluid ($m^2/s$) |
| $\gamma_m$, $m = 1, 2$ | normalized total viscosities |
| $\lambda_{ci}$ | Swirling strength of turbulent flow (1/s) |
| $\nu$ | Kinematic viscosity of fluid ($m^2/s$) |

| | |
|---|---|
| $\nu_s$ | Sub-grid viscosity ($m^2/s$) |
| $\sigma_m$, $m = 1, 2$ | Ratio of grid intervals |
| $\Theta$ | Normalized temperature |

## 1 Introduction

Turbulence is widely existed in nature and industrial flows, usually occurs at large Reynolds numbers [1]. When a flow is turbulent, the heat, mass, and momentum transport generally occurs at a greater rate as compared with the corresponding rate of transportation in the molecular level. Furthermore, turbulence brings about the difficulty of reaction rate determination, as can be seen in the work of modeling and simulation carried out by Betelin, Smirnov et al. [2]. Turbulence prediction is essential in many engineering designs that involve the calculations of aerodynamic forces and heat and mass transfer. Therefore, the turbulent air natural-convection in a differentially heated square cavity should be a benchmark problem in thermo-hydrodynamics.

Natural-convection in rectangular enclosures has been studied extensively due to its wide engineering applications, such as building ventilation and air conditioning, cooling of electronic devices and solar collectors, and nuclear reactor sub-systems. In recent years, experiments have been carried out to investigate the laminar air natural-convection in a square cavity with a heating strip by a two-dimensional particle image velocimetry (PIV) system [3], and the turbulent air natural-convection in a differentially heated square cavity by systems with micro-thermocouples and a Laser Doppler Anemometer (LDA) [4–6]. For the measurement of air natural-convection in a cavity at large Rayleigh numbers (on the order of $10^{11}$), Saury et al. [7] have built a large-scale experimental setup, which has a height of 4m with a horizontal cross-section of $0.86 \times 1.00\,m^2$. They analyzed the airflow inside the cavity, and presented the Nusselt number along the hot and cold walls.

While recent numerical simulations have the object of exploring the second largest Lyapunov exponent and transition to chaos of natural-convection in a rectangular cavity [8], the characteristics of laminar natural-convection in a closed square cavity with special heating modes [9–11] or with special numerical approach [12, 13], the heat transfer by natural convection in an inclined cavity with a wavy heating side wall [14], and the interaction of natural-convection and surface thermal radiation in inclined square enclosures [15].

A brief literature view of natural-convection in a rectangular cavity was given in our previous work [16], in which the eddy viscosity type k-$\epsilon$ model was employed. The k-$\epsilon$ model cannot satisfactorily predict the turbulent quantities, such as the root mean square of velocity components and temperature.

For turbulent flow simulations, the three strategies such as the phenomenological models, large eddy simulations (LES) and direct numerical simulation with Navier Stokes equations (DNS) are widely used. The phenomenological type one-point closure models for buoyancy-driven turbulent flows have been reviewed by Hanjalic [17]. These models have three types: eddy-diffusivity models, algebraic flux models and those with second moment closures. They were proposed from Reynolds averaging, but the lacking of universal property for the model coefficients implies that these coefficients examined in some benchmark situations might be unsuitable to other relatively complicated engineering problems, although computational results for many cases agree with experimental data rather well. Therefore, the one-point closure models is just a good solution marker in engineering turbulent flow problems, since the underlying physical mechanism has not been sufficiently emphasized, and usually the higher order moments have to be approximated by lower ones to solve the non-closure problem from averaging.

Direct numerical simulation (DNS) [1, 18–20], in the traditional meaning, should use extremely fine grids so that the total spatial grid numbers should be as large as $Re^{2.25}$, here Re is the Reynolds number. This indicates that super computers must be used in DNS of fully developed turbulent flows. For instance, a set of complete two- and three-dimensional DNS of air natural-convection in a differentially heated cavity of aspect ratio 4 with adiabatic horizontal walls was carried out by Trias et al. [21]. It was reported that there exist significant differences between two- and three dimensional results, which become more marked at the highest Rayleigh number. Furthermore, they also presented the results of a set of complete DNS of air natural-convection in a differentially heated cavity of aspect ratio 4 and Ra up to $10^{11}$ in two parts [22, 23], including the time averaged flow results, the heat transfer, and the flow dynamics.

Large-eddy simulations (LES) [24, 25] adopt grid-filtering to simulate the large motion explicitly, while the small eddy effect on the large eddy motion should be modeled physical-mathematically. For instance, for the simulation of turbulent thermal flows, a non-linear sub-grid scale (SGS) heat flux model was introduced and used by Peng and Davidson [26]. The proposed non-linear model accounts for the SGS heat flux in terms of the large-scale strain-rate tensor and temperature gradients. They have also carried out LES of air natural-convection in a square cavity at Ra = $1.58 \times 10^9$, and obtained a good agreement with experimental data [27]. The LES work reported previously [28–48] indicates LES is an appropriate strategy for predicting turbulent flows.

It is noted that for LES a sub-grid scale model based on the Kolmogorov equation for resolved turbulence was proposed by Cui et al. [36, 37]. A local sub-grid diffusivity model for the large eddy simulation of natural-convection flows in cavities was developed by Sergent et al. [39]. This model does not use the Reynolds analogy with a constant sub-grid Prandtl number, but computes the sub-grid diffusivity independently by using the mixed-scale model [40]. They reported that the sub-grid diffusivity has a strong influence the transition to turbulence in the wall layer.

For natural-convection boundary layer in a cavity with an aspect ratio of 5 at a Rayleigh number of $4.028 \times 10^8$, Barhaghi and Davidson [41] have conducted a LES work, and found that the dynamic sub-grid scale model is the most accurate in terms of predicting the transition location. The accuracy of the results in the transition region is highly grid dependent, indicating that the sub-grid scale fluctuations in the transition region are of different nature compared to the fully turbulent region. As expected previously [38], LES is the most suitable for unsteady three-dimensional complex turbulent flows in industry and natural environment.

Even though in LES the unclosed stresses are usually modeled by SGS-viscosity models, alternatively, to smooth the dynamics of the Navier-Stokes equations, another way is to directly modify the non-linear convective terms [42]. Thus, models based on these regulations occur. The Leray-$\alpha$ model [43–45] is the simplest regularization model, for which Reeuwijk et al. [46] have assessed its potential in modeling wall-bounded flows, such as the air flow in a side-heated vertical channel at $Ra = 5 \times 10^6$. In addition, a parameter-free symmetry-preserving regularization modeling of natural-convection in a turbulent differentially heated cavity was presented by Trias et al. [47], where the $C_4$-regularization of the non-linear convective term (as seen in [48]) was considered as a simulation shortcut. Basically, the regularization method alters the non-linearity to restrain the production of small scales of motion [44]. The so-called parameter free means no constant needs to be tuned or prescribed in advance.

This paper presents the LES results of turbulent air natural-convection in a differentially heated square cavity at a Rayleigh number of $5.33 \times 10^9$. In the LES work, the SGS model is given by a non-dimensional analysis where the swirling strength and the harmonic average grid interval are used as primary variables. A factor of swirling strength intermittency (FSI) is defined by the ratio of the swirl strength to the magnitude of the complex eigenvalue of the filtered velocity gradient tensor. It is used instead of the near-wall length scale decaying factor. The air natural convection in the square cavity is considered as mixed by both the non-swirling and swirling regimes.

The air flow in the square cavity can be simply partitioned to the loop wall jet near the walls and the flow in the core region. In a turbulent regime, the air flow in the cavity is intermittent in time and space, the flow may be swirling or non-swirling, depending on if the swirling strength exists. The SGS model described in this paper can to some extent reflect this flow property. The results of the LES are compared with existing experimental data.

## 2 Governing equations

At higher Reynolds numbers, sub-grid scale effect on large scale motions should be considered carefully. In previous LES work [28–48], sub-grid stress is usually assumed to be the product of the eddy viscosity and the strain rate locally filtered is just an analogy to the constitutive relationship in Newtonian fluid mechanics. The sub-grid scale model used in these LES work hasn't successfully ascertained at which Reynolds number the LES sub-grid scale model should be applicable: the effect of the sub-grid viscosity is still remained, even when the flow turns to laminar state and the swirling strength becomes zero in general scenarios (i.e., in flows without Coriolis force effect).

In the earlier work of Smagorinsky [28], the sub-grid viscosity is assumed to be proportional to the modular of local strain rate of filtered velocity field. Unfortunately, using the three-dimensional velocity fields based on flow instability analysis [49], it is convenient to verify by numerical test that the peak values of the modular of strain rate occurs at regions without swirling. Therefore, the sub-grid viscosity in Smagorinsky's form should exist in shear flow without swirling, which is clearly non-practical. To overcome this ambiguity, considering turbulent flow contains coherent structures, here we suggest a sub-grid scale model where the sub-grid viscosity is proportional to the FSI based on the filtered local velocity gradient. As reported elsewhere [50], the present SGS model suggests the SGS viscosity $v_s$ be expressed as

$$v_s = C_\mu f_I(\mathbf{x}, t)\lambda_{ci}\delta^2 \tag{1}$$

Here $C_\mu (= 0.09)$ is an artificially defined constant. Note that both choice of $C_\mu$ value and the selective strategy of length scale $\delta$ have direct effects on the sub-grid viscosity. $\lambda_{ci} (\geq 0)$ is the swirling strength of the filtered velocity gradient $\nabla\mathbf{u}$. The FSI, $f_I$, is defined by the ratio of swirling strength to the magnitude of the complex eigenvalue $\lambda (= \lambda_{cr} + i\lambda_{ci})$ of velocity gradient tensor $\nabla\mathbf{u}$. This means

$$f_I(\mathbf{x},t) = \frac{\lambda_{ci}}{\sqrt{\lambda_{cr}^2 + \lambda_{ci}^2}} \tag{2}$$

The length scale $\delta$ is assumed to be the harmonic average of grid interval, which is defined by

$$\frac{1}{\delta} = \sum_{i=1}^{3} 1/\delta_i \tag{3}$$

giving a larger weight to the smaller grid interval, with $\delta_i$ denoting the grid interval in the $x_i$ direction. If the filtered velocity gradient $\nabla \mathbf{u}$ is denoted by

$$\nabla \mathbf{u} = \mathbf{A} = \begin{pmatrix} a_{11} & a_{12} & a_{13} \\ a_{21} & a_{22} & a_{23} \\ a_{31} & a_{32} & a_{33} \end{pmatrix} \tag{4}$$

its eigenvalue $\lambda$ must satisfy the characteristic equation

$$\lambda^3 + b\lambda^2 + c\lambda + d = 0 \tag{5}$$

where

$$\begin{cases} b = -\mathrm{tr}(\mathbf{A}) = -(\mathrm{a}_{11} + \mathrm{a}_{22} + \mathrm{a}_{33}), \\ c = \begin{vmatrix} a_{22} & a_{23} \\ a_{32} & a_{33} \end{vmatrix} + \begin{vmatrix} a_{11} & a_{12} \\ a_{21} & a_{22} \end{vmatrix} + \begin{vmatrix} a_{11} & a_{13} \\ a_{31} & a_{33} \end{vmatrix}, \quad d = -|\mathbf{A}| \end{cases} \tag{6}$$

with $|\mathbf{A}|$ representing the determinant of matrix $\mathbf{A}$. It is noted that for any incompressible flow, the value of parameter $b$ in Eqs. (5–6) is exactly zero, since the flow should be divergence free. If the flow is at a laminar regime excluding the instable situations and those in the rapidly rotating frames, the roots of Eq. (5) are in general real; while when the flow is at a turbulent regime, the roots must have two conjugate complex eigenvalues denoted by $\lambda_{cr} \pm i\lambda_{ci}$, here $i(=\sqrt{-1})$ is the unit of imaginary number. The iso-surfaces of swirling strength have been used to illustrate vortices in turbulent flows previously [51–53].

It is worth noting that the value of $C_\mu$ is set as 0.09, which is the same as that of $C_\mu$ used to define turbulent eddy viscosity in phenomenological type one-point closure models [17]. Here we tend to use the harmonic average to define the length scale of grid interval $\delta$, since any smaller grid interval can get a larger weight of average. This of course has affected on the calculation of SGS viscosity, but just in the value. In principle, we suggest that the local SGS viscosity be vanished when $\lambda_{ci} = 0$, therefore, leading to a natural lapse of LES to DNS.

In the present study, the sub-grid viscosity $v_s$ has a factor $f_I$, which is used instead of the near-wall length scale decaying factor $[1 - \exp(-y^+/25)]$ as used in previous LES work [29], where $y^+ = yu_\tau/v$, $y$ denotes the normal distance to the wall, with $u_\tau$ denoting the mean friction velocity and $v$ representing the kinematic viscosity of fluid.

It should be noted that the swirling strength can occur in laminar flows when there exists the Coriolis force effect due to coordinate rotation. To observe the difference in different sub-grid models in some detail, a comparison of the present sub-grid model with that described previously by Vreman [54] is given in Fig. 1a, b, where two top-views of the contours of sub-grid viscosity are shown. It is seen that the sub-grid viscosity based on the present model is zero if the flow is non-swirling, while the sub-grid viscosity based on the Vreman's model doesn't hold this peculiarity.

Consider the natural-convection in a square cavity in a Cartesian coordinate system, in which $x$ is the horizontal coordinate, with y and z denoting the vertical and spanwise directions. The origin is set at the center of the cavity with a length-height-depth ratio of 1:1:2, and the spanwise coordinate is merely denoted by the symbol $z$. For the problem considered, a schematic is depicted in Fig. 2, where the square cavity is differentially heated and air-filled, the kinematic viscosity and thermal diffusivity of air are denoted by $v$, and $\kappa$, respectively. Buoyancy results in a clockwise flow in the mid plane ($z = 0$) because of the heat transfer from the left hot wall with temperature $T_h$ to the right cold wall with temperature $T_c$. The horizontal walls are conductive. Their temperatures are assigned with respect to measured data. It is assumed that the front and rear vertical walls are adiabatic, and the Boussinesq approximation of buoyancy is valid and can be used to simplify the momentum equations.

Let $\Delta T = T_h - T_c$, $\rho_0$ be the air density at temperature $(T_h + T_c)/2$, and $\beta_T$ be the coefficient of volumetric expansion of fluid, following the approach of Wakitani [55], we choose $W_0 = \sqrt{g\beta_T H \Delta T}$ and the cavity height $H$ as the velocity and length scales, hence the time and pressure scales should be $t_0 = H/W_0$ and $\rho_0 W_0^2$. Let $\Theta = [T_h - (T_h + T_c)/2]/\Delta T$, the dimensionless governing equations for the turbulent natural-convection problem can be written as:

$$\nabla \cdot \mathbf{u} = 0 \tag{7}$$

$$\mathbf{u}_t + \mathbf{u} \cdot \nabla \mathbf{u} = -\nabla p + \Theta \mathbf{e_2} + \nabla \cdot [\gamma_1 \nabla \mathbf{u}] + \mathbf{R} \tag{8}$$

$$\Theta_t + \mathbf{u} \cdot \nabla \Theta = \nabla \cdot [\gamma_2 \nabla \Theta] \tag{9}$$

where $\mathbf{e_2} = (0, 1, 0)$ is the unit vector in the vertical direction, and $\Pr(= v/\kappa)$ is the Prandtl number of air which has a value of 0.71, with the Rayleigh number defined by $Ra = g\beta_T H^3 \Delta T/(v\kappa)$. For the expressing simplicity, here we have omitted the over bar for filtering of variables. Let $\mathrm{Re} = (Ra/\Pr)^{0.5}$, then the normalized total viscosity $\gamma_1$ can be represented by

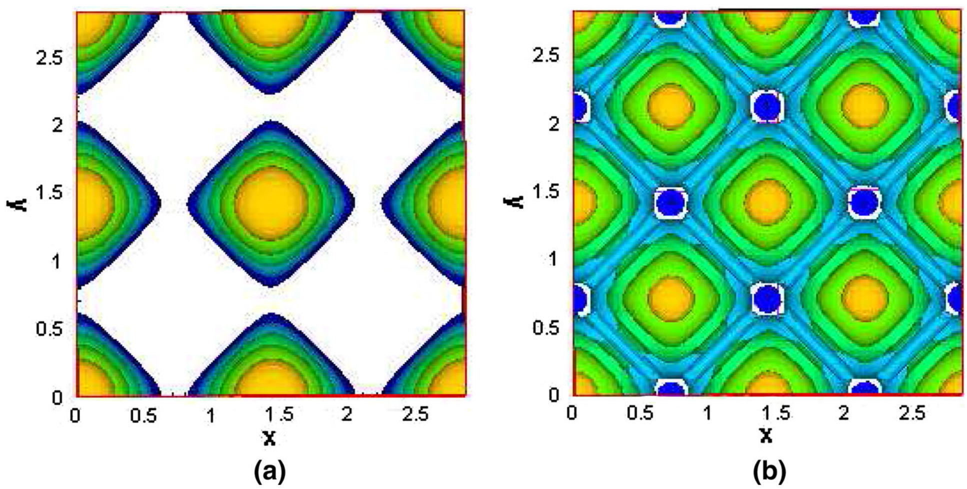


**Fig. 1** Comparison of the sub-grid scale model with that proposed by Vreman [54]. **a** A *top-view* of the contours of $v_s$ based on the present model; **b** A *top-view* of the contours of $v_s$ based on the Vreman's model. Note that the sub-grid viscosity has a unit of $W_0 d$ as seen in "Appendix". The contours in **a** are labeled by values from 0.0004 to 0.0016 with an increment of 0.0003, while the contours in **b** are labeled by values from 0.0004 to 0.012 with an increment of 0.0029

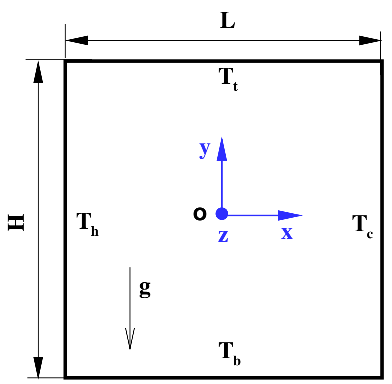


**Fig. 2** Schematic of turbulent air natural-convection in a differentially heated square cavity

$$\gamma_1 = \frac{1}{\mathrm{Re}}\left(1 + \frac{v_s}{v}\right) \tag{10}$$

with

$$\gamma_2 = \frac{1}{\mathrm{Re}\ \ \mathrm{Pr}}\left(1 + \frac{v_s}{\sigma_\theta v}\right) \tag{11}$$

where the turbulent Prandtl number $\sigma_\theta$ is assumed to be 0.9, which is the same as that previously used in eddy viscosity type k-$\epsilon$ model [16]. **R** denotes a force depending on viscosity gradient,

$$\mathbf{R} = (\nabla \mathbf{u})^T \cdot \nabla \gamma_1 \tag{12}$$

On the cavity walls, the air flow is non-slip, $\mathbf{u} = \mathbf{0}$. On the front and rear walls, the adiabatic condition for $\Theta$ was used, that means, $\partial\Theta/\partial z = 0$, for $z = \pm 1$. As schematically shown in Fig. 2, the boundary condition for $\Theta$ on the left hot wall is

$$\Theta = 0.5, \mathrm{for\,x} = -0.5, \mathrm{y} \in (-0.5, 0.5), \mathrm{z} \in (-1, 1) \tag{13}$$

On the right cold wall, it becomes

$$\Theta = -0.5, \mathrm{for\,x} = 0.5, \mathrm{y} \in (-0.5, 0.5), \mathrm{z} \in (-1, 1) \tag{14}$$

**Table 1** The measured $\Theta$ on the top and bottom walls as a function of $x$

| $x$ | $\Theta_b$ | $\Theta_t$ | $x$ | $\Theta_b$ | $\Theta_t$ |
|---|---|---|---|---|---|
| −0.5 | 0.5 | 0.5 | 0.1 | −0.1705 | 0.108 |
| −0.492 | 0.3977 | 0.4318 | 0.2 | −0.2045 | 0.0567 |
| −0.4885 | 0.3693 | 0.4205 | 0.25 | −0.225 | −0.0378 |
| −0.475 | 0.3409 | 0.4148 | 0.3 | −0.245 | 0 |
| −0.451 | 0.2655 | 0.3611 | 0.34 | −0.2557 | −0.0568 |
| −0.409 | 0.1468 | 0.3182 | 0.409 | −0.3182 | −0.1704 |
| −0.34 | 0.0205 | 0.2557 | 0.451 | −0.3977 | −0.2841 |
| −0.3 | 0 | 0.235 | 0.475 | −0.4148 | −0.3636 |
| −0.25 | 0.02045 | 0.2222 | 0.4885 | −0.4205 | −0.3693 |
| −0.2 | −0.06818 | 0.2045 | 0.492 | −0.4318 | −0.3977 |
| −0.1 | −0.1136 | 0.1704 | 0.5 | −0.5 | −0.5 |
| 0 | −0.1407 | 0.1307 | | | |

It is noted that on the top and bottom walls, the value of $\Theta$ is linearly interpolated with measured data given in Table 1 [5].

## 3 Numerical method

The governing Eqs. (7–9) of the natural-convection in a square cavity were discretized by a finite difference method in a non-uniform staggered grid system, where the convective terms were dealt with a fourth order upwind scheme [56], which has been used to study turbulent heat and fluid flows at higher Reynolds numbers [57]. The gradients $\nabla\gamma_1$, and $\nabla\gamma_2$ were treated using a second order central difference scheme. By some proper changes, the existing numerical methods in DNS, as those reported previously [58–61], should also be applicable in LES. It is noted that recently Trias et al. [62] have reported a simple numerical approach to discretize the viscous term with spatially varying viscosity, which can be implemented easily on any structured or unstructured grid, is of course also suitable for LES of incompressible flows.

The solutions of the Eqs. (7–9) are sought by the accurate projection algorithm named for PmIII [63]. The using procedure of the projection algorithm was described elsewhere [64]. Due to the further use of the sub-grid scale model, it is necessary to repeat similarly.

Let the intermediate velocity vector, the pressure potential and the time level be denoted by $\bar{\mathbf{u}}$, $\phi$ and $n$, respectively. Assume $\mathbf{H} = [(\mathbf{u}\cdot\nabla)\mathbf{u} - \mathbf{R} - \Theta\mathbf{e_2}]$, then let

$$\mathbf{u}^{n+1} = \bar{\mathbf{u}} - \Delta t\nabla\phi \tag{15}$$

we can calculate $\bar{\mathbf{u}}$ by

$$\frac{\bar{\mathbf{u}} - \mathbf{u}^n}{\Delta t} + \mathbf{H}^{n+1/2} = \nabla\cdot\left\{\gamma_1\nabla[\mathbf{u}^n + \frac{1}{2}(\bar{\mathbf{u}} - \mathbf{u}^n)]\right\} \tag{16}$$

and calculate pressure $p$ by

$$p^{n+1/2} = \{1 - 0.5\Delta t\nabla\cdot[\gamma_1\nabla]\}\phi \tag{17}$$

where the pressure potential $\phi$ must satisfy the Poisson's equation

$$\nabla^2\phi = \nabla\cdot\bar{\mathbf{u}}/\Delta t \tag{18}$$

while the temperature $\Theta^{n+1}$ can be calculated by

$$\frac{\Theta^{n+1} - \Theta^n}{\Delta t} + H_4^{n+1/2} = \nabla\cdot\left\{\gamma_2\nabla[\Theta^n + \frac{1}{2}(\Theta^{n+1} - \Theta^n)]\right\} \tag{19}$$

where $H_4 = \mathbf{u}\cdot\nabla\Theta$, and the terms at the level of $(n + 1/2)$ are calculated explicitly using a second order Euler predict-correction scheme in time. The pressure potential Poisson's equation is solved by the approximate factorization one (AF1) method [65]. The criterion for pressure potential iteration was chosen so that the relative error defined previously [66] should be less than $10^{-9}$. The temperature Eq. (19) is solved by time marching. The implicit second-order Crank-Nicolson was used to numerically deal with the right-hand side diffusion terms. Note that the numerical method has a nonstandard treatment of the viscous dissipation term, where the part depending on the viscosity gradient $(\nabla\gamma_1)$, as denoted by $\mathbf{R}$ in Eq. (12) is calculated explicitly, while the remainder part denoted by $[\nabla\cdot(\gamma_1\nabla\mathbf{u})]$ is calculated implicitly.

It is noted that the velocity $v_{ijk}$ is stored in the grid point $(x_i, y_{j-1/2}, z_k)$ due to the staggered grid arrangement, there exists a prediction of $\Theta_{j-1/2}$ in the the prediction of $H_2$. In the present LES, the following third-order upwind scheme

$$\Theta_{j-1/2} = \begin{cases} \Theta_{j-1} + A_1(\Theta_{j-1} - \Theta_{j-2}) + B_1(\Theta_{j-1} - \Theta_j) & \text{for } v_j > 0 \\ \Theta_j + A_2(\Theta_j - \Theta_{j+1}) + B_2(\Theta_j - \Theta_{j-1}) & \text{for } v_j \le 0 \end{cases} \tag{20}$$

is used. For $\delta y_j = y_j - y_{j-1}$, let $\sigma_1 = \delta y_j/\delta y_{j-1}$, $\sigma_2 = \delta y_j/\delta y_{j+1}$, the coefficients in the scheme derived from the Taylor expansion can be expressed as $B_m = \frac{2+\sigma_m}{4(1+\sigma_m)}$, $A_m = \frac{1}{2}\sigma_m(1 + 2B_m)$, for m = 1, 2.

## 4 Results and discussion

Using the numerical method described in the foregoing section, for the natural-convection in a square cavity as schematically shown in Fig. 2, a LES was carried out in a personal computer with a memory of 1 Gb. The CPU time for the LES in the time period $t \in (90, 180)$ is about 53 h. The square cavity has a ratio of length to height to depth of 1:1:2, as reported in the experimental studies [5, 6]. Nearly uniform spanwise grid had a grid number of 121, that means the 10 z-directional meshes near the rear wall were amplified gradually by a factor of 1/0.975, while the 10 z-directional meshes near the front wall were shortened gradually by a factor of 0.975, the meshes in the central region were uniform. The minimum and maximum grid intervals were, respectively, 0.01322 and 0.017029.

Non-uniform horizontal and vertical grids had the same grid number of 101. There were 39 non-uniform meshes near the top, bottom, heating, or cooling wall, the mesh lengths from the wall to the central region were amplified gradually by a factor of 1/0.88 or 1/0.86317. Therefore, when the amplifying factor is 1/0.88, the minimum and maximum grid intervals are respectively $2.015 \times 10^{-4}$, and 0.02594; when the amplifying factor is 1/0.86317, the relevant minimum and maximum grid intervals are $1.0198 \times 10^{-4}$, and 0.0273451. For $\mathrm{Rc} = Ra/10^9 = 5.33$, the Reynolds number $[\mathrm{Re} = (Ra/\mathrm{Pr})^{0.5}]$ is 86661, the minimum $\delta y$ denoted by $(\delta\hat{y})min[= (\delta y)min\cdot \mathrm{Re}]$ is 17.463 for the amplifying factor 1/0.88, or 8.838 for the amplifying factor 1/0.86317.

Numerical results' evaluation involved with the grid adjustment in $x$ and $y$ directions was done by simply showing the evolutions of the face-mean Nusselt numbers on the left and right walls, as indicated in Fig. 3. The grid adjustment does have observable influence on the evolutional orbits. However, from the point of time averaging, the impact of grid adjustment is negligible. It is noted that when the $(\delta\hat{y})min$ is adjusted from 17.463 to 8.838, the time step $\Delta t$ has to be changed from $2.25 \times 10^{-3}$ to $1.75 \times 10^{-3}$. Nevertheless, we tend to report the LES results of natural-convection in a square cavity at $\mathrm{Rc} =$ 5.33 for the scenario of $(\delta\hat{y})min = 8.838$, and $\Delta t = 1.75 \times 10^{-3}$.

### 4.1 Turbulence statistics

The evolutions of velocity components at the four near-wall monitoring points ($P_i, i = 1, \ldots, 4$) in the mid plane ($z$ = 0) are shown in Fig. 4. The irregular velocity fluctuation suggests that the natural convection in the cavity at $Ra = 5.33 \times 10^9$ (or Rc = 5.33, Re = 86661) is certainly turbulent. The behavior of velocity evolution is similar to that observed in experiments [6], although the point locations are different.

The time-averaged velocity profiles in the mid plane ($z$ = 0), together with the profiles at Rc = 1.58, are given in Fig. 5, in which part (a) illustrates the v-profile near the left heating wall, with part (b) indicating the u-profile on the vertical centerline. These velocity profiles are in a good agreement with experimental data obtained at Rc = 1.58 [5]. This comparison indicates that the Rayleigh number has some influence on the velocity profiles in the mid plane ($z$ = 0).

The temperature evolutions at the three near-wall points ($P_1, P_3, P_4$) in the mid plane ($z$ = 0) are shown in Fig. 6. It was found that, at $P_1$, $\hat{x} = 0.03 \cdot$ Re $\approx 2600$, the temperature fluctuates at a mean value close zero is not strange, since $P_1$ is far from the vertical jet near the left heating wall and is certainly located in the core region. While at $P_3$ and $P_4$, the mean temperatures are respectively positive and negative, mainly caused by the effects of heating and cooling from the left and right walls.

A comparison of the $\Theta_{av}$ profiles with experimental data [5] is given in Fig. 7a, b. As shown in Fig. 7a, the Ra influence on the vertical $\Theta_{av}$ profile is observable, but slightly smaller than the horizontal $\Theta_{av}$ profile (Fig. 7b). Comparing the $\Theta_{av}$ profiles along the centerlines of mid plane ($z$ = 0), it indicates that in the present LES, the assigned $z$-independence of the temperature on horizontal walls may be partially inconsistent with the practical

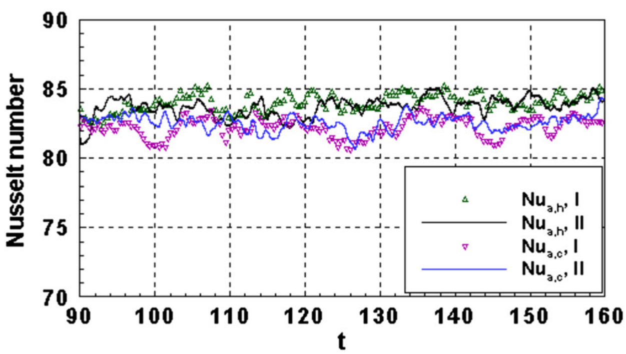


**Fig. 3** Evolutions of the face-mean Nusselt numbers on the *left* and *right* walls. Note that in the legend, the symbol I represents the grid in the case of $(\delta\hat{y})min = 17.46$ is used, with the symbol II relevant to the grid scenario $(\delta\hat{y})min = 8.838$

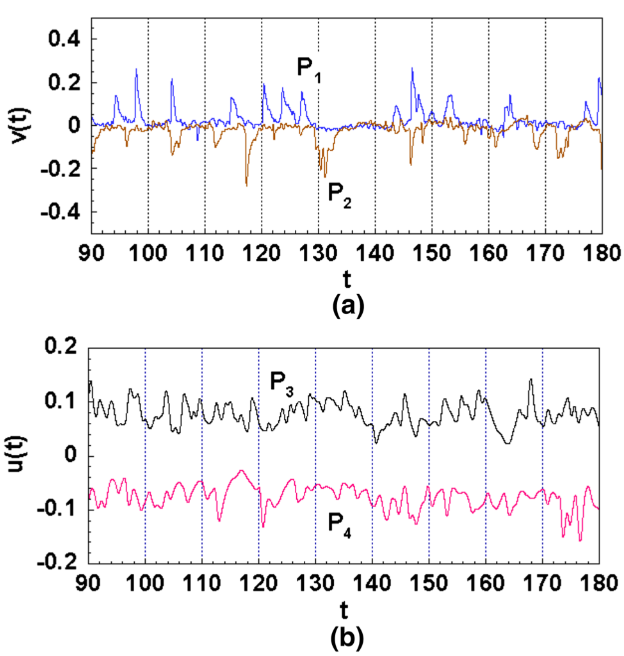


**Fig. 4** Evolution of velocity components at four different points near walls in the mid plane ($z$ = 0). **a** Vertical velocity; **b** horizontal velocity. Note that the four monitoring points are given by $P_1(-0.47, 0, 0)$, $P_2(0.47, 0, 0)$, $P_3(0, 0.47, 0)$ and $P_4(0, -0.47, 0)$

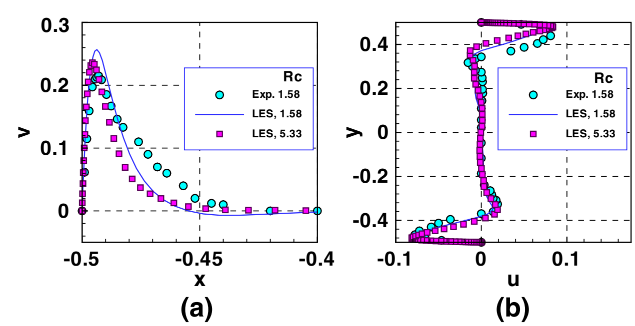


**Fig. 5** Comparison of the time-averaged velocity components near the *left hot wall* on the *horizontal centerline* (**a**) and *vertical centerline* (**b**) in the mid plane ($z$ = 0) with experimental data

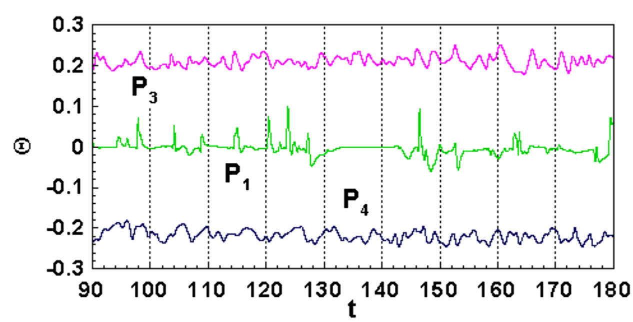


**Fig. 6** Evolution of temperature at three different points near walls in the mid plane ($z$ = 0). The coordinates of points are the same as in Fig. 3

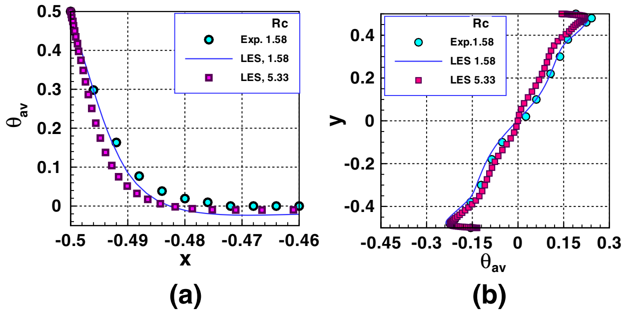


**Fig. 7** Comparison of the time-averaged temperature near the *left hot wall* on the *horizontal centerline* (**a**) and the *vertical centerline* (**b**) in the mid plane ($z = 0$) with experimental data

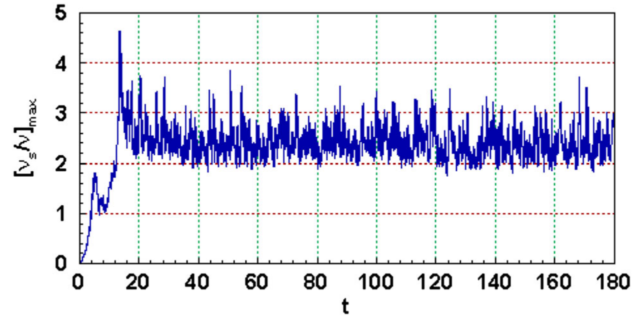


**Fig. 10** Evolution of maximum viscosity ratio, $(v_s/v)max$, in the cavity

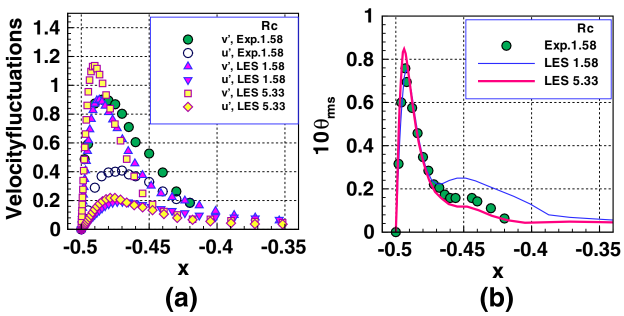


**Fig. 8** Comparison of the root mean square (rms) of velocity components (**a**) and temperature (**b**) near the *left hot wall* in the mid plane ($z = 0$) with experimental data. Note that the rms of velocities have multiplied by a factor of $Ra^{0.05}W_0/v_{\max}$

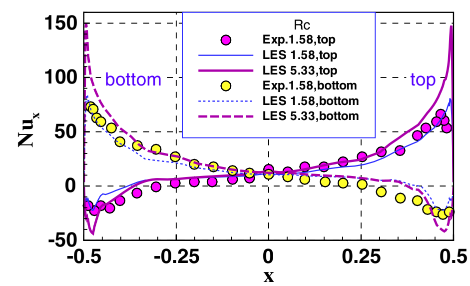


**Fig. 11** Comparison of the t-z averaged Nusselt number on the *bottom* and *top walls* with experimental data

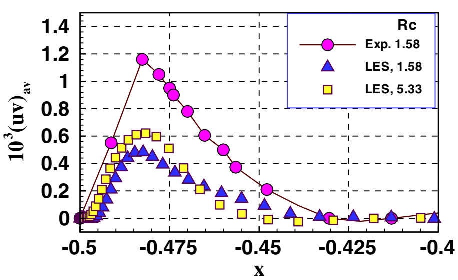


**Fig. 9** Comparison of the Reynolds shear stress distribution along the *horizontal centerline* in the mid plane ($z = 0$) with experimental data

measurement of Tian and Karayiannis [5, 6]. In Fig. 7b, it is seen that the $\Theta_{av}$ profile along the vertical centerline agrees relatively well with the measured data.

The root mean square (rms) of velocity components $(u', v')$ and temperature $(\Theta')$ near the left hot wall in the mid plane ($z = 0$) are compared with the experimental data [6], as shown in Fig. 8a, b. Both of the $v'$ and $\Theta'$ agree well with the measured data, with the effect of Rayleigh number remained observable. But the $u'$ is obviously under-predicted, which may evidently cause the under-prediction of turbulent shear stress near the heating wall (Fig. 9).

For maximum viscosity ratio in the cavity denoted by $(v_s/v)max$, its evolution of can be seen in Fig. 10. Because the maximum viscosity ratio is closely related to the motion and the mutual interaction of large eddies caused by the differentially heating of air, the location of $(v_s/v)max$ in the cavity must be varied instantaneously. For the natural-convection in a cavity at Rc $= 5.33$, the maximum viscosity ratio $[(v_s/v)max]$ oscillates around 2.403 with a rms value of about 0.293, if a statistical analysis is made merely for the evolution data in the time range $t \in (90, 160)$.

## 4.2 Nusselt numbers

The face-mean Nusselt numbers, with the evolutions of those on the left and right walls shown in Fig. 3, again exhibit the oscillating properties. The time-face averaged Nusselt numbers on the bottom and top walls, as shown in Fig. 11, are respectively about 18.46, and 18.95. The heat flow is transferred into the cavity from the bottom wall and out of the cavity from the top wall. The two predicted values of the Nusselt numbers on the bottom and top walls at Rc $= 5.33$, are slightly larger than the measured data (14.97 and 15.67) for the case Rc $= 1.58$ [5]. The time-face averaged Nusselt numbers on the left hot and right

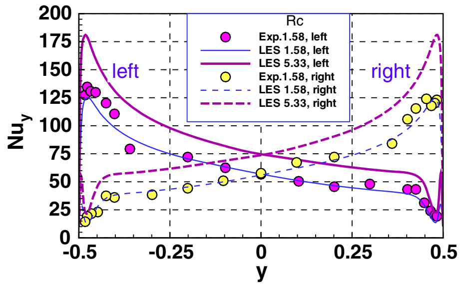


**Fig. 12** Comparison of the t-z averaged Nusselt number on the *left* and *right walls* with experimental data

cold walls, as shown in Fig. 12, are respectively 83.86 and 82.63. The two values agree well with the numerically obtained expression given by Fusegi et al. [67]

$$\overline{Nu} = 0.163Ra^{0.282} \tag{21}$$

with a relative discrepancy of about 8 %.

In Fig. 11, it is seen that the increase of Rc has enhanced evidently the heat transfer rates from the horizontal wall, when the normalized horizontal wall temperatures are assumed to be $z-$ independent, and assigned by the linear interpolation based on Table 1. While the heat transfer rates from the left hot and right cold walls, as seen in Fig. 12, are to some extent consistent with the numerical results of Fusegi et al. [67], the present LES has slightly under-predicted with a relative discrepancy mentioned above. From these comparisons, it reveals that the heat transfer rates caused by the natural-convection in a square cavity may be sensitive to the horizontal wall temperature assignment. When the Rayleigh number is relatively large, the surface thermal radiation effect on the heat transfer in a square cavity may become crucial [15].

## 4.3 Flow patterns

The flow patterns of natural-convection in the square cavity at three instants in the mid plane are given by the contours of vorticity $\omega_z$, as shown in Fig. 13a–c. Affected

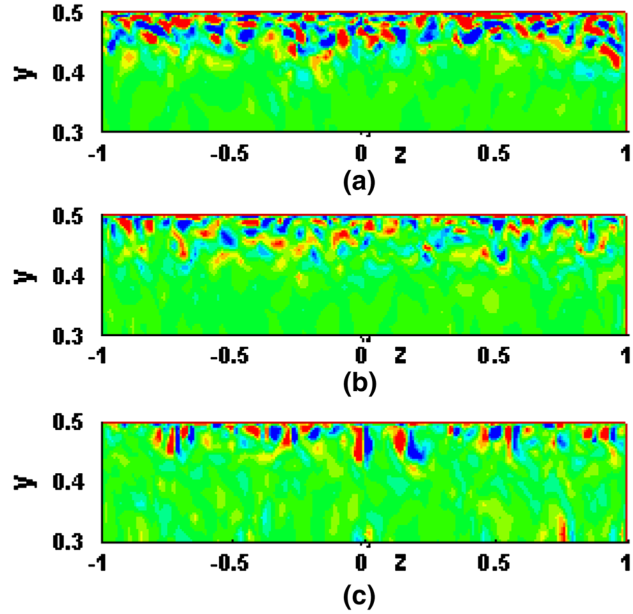


**Fig. 14** Instantaneous secondary flow patterns near the top wall illustrated by contours of $\omega_x$. **a** $x = -0.25$; **b** $x = 0$; and **c** $x = 0.25$. Note that the contours of $\omega_x$ are labeled by the same values as given in Fig. 13

by the square cavity corners, the loop wall jet has to turn directions. Accompanying the loop wall jet, series vortices occur in the regions related to the square core region, which, is separated from the cavity walls by the loop wall jet. The shapes of these vortices vary in time and space due to the wall effect and their interaction.

To show the secondary vortical structures near the top wall at $t = 175$, the contours of $\omega_x$ in three planes are shown in Fig. 14a–c. The three flow structures near the top wall are relevant to the pattern given in Fig. 13c. Influenced by the left wall heating and the left-top corner, the secondary flow structures near the top wall at $x = -0.25$ (Fig. 14a) is more complex than those in other two planes, as seen in Fig. 14b, c. Similarly, as seen in Fig. 15a–c, impacted by right wall cooling and the right-bottom corner, the secondary flow structures near the top wall at $x = 0.25$ (Fig. 15c) is more complex than those given in Fig. 15a, b.

**Fig. 13** Instantaneous secondary flow patterns in the mid plane ($z = 0$) illustrated by contours of $\omega_z$. **a** $t = 157.5$; **b** $t = 166.25$; and **c** $t = 175$. The labeled range of $\omega_z$ is from $-2$ to 2, with an increment of 0.4

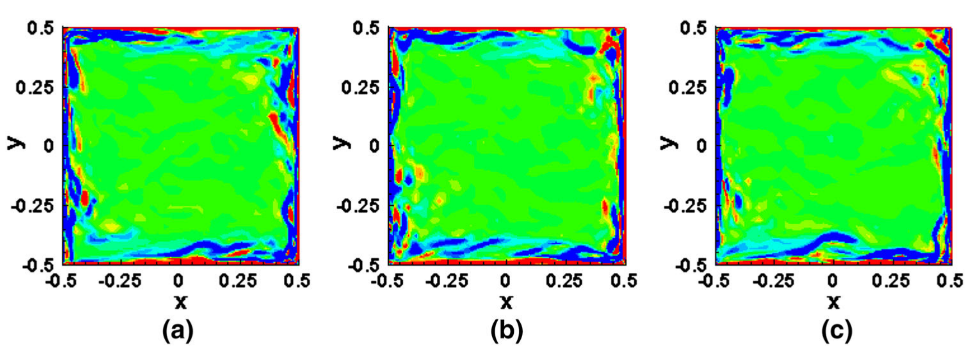

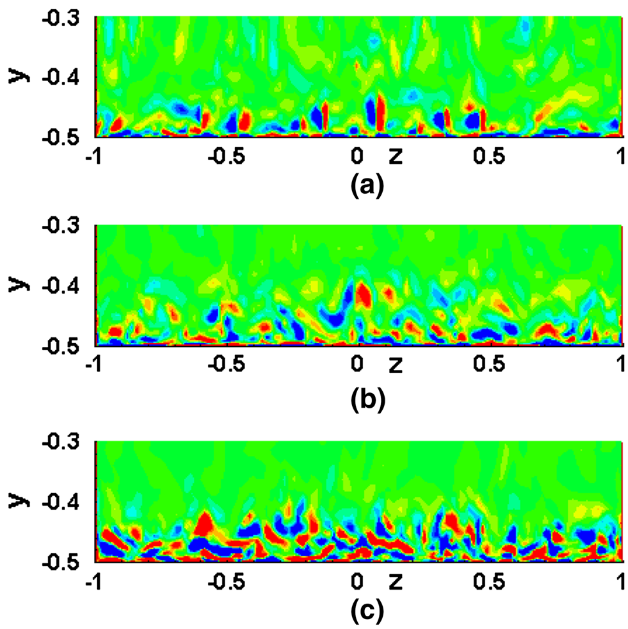


**Fig. 15** Instantaneous secondary flow patterns near the bottom wall illustrated by contours $\omega_x$. **a** $x = -0.25$; **b** $x = 0$; and **c** $x = 0.25$. Note that the contours of $\omega_x$ are labeled by the same values as given in Fig. 13

## 4.4 Intermittent behaviors

The iso-surfaces of the FSI in the 1/8 domain of simulation at $t = 180$ are shown in Fig. 16a. As seen in Eq. (2), the spatial distribution of FSI is obviously dependent on the swirling motion, which is quantified by the swirling strength $\lambda_{ci}$ [51]. The swirling strength ($\lambda_{ci}$) varies intermittently in time and space, since the flow is in a regime of week turbulence at $Rc = 1.58$ and 5.33, indicating that turbulent intermittence certainly occur in buoyancy-driven flows in the cavity. In the core region of the cavity, even though the FSI does not vanish, the viscosity ratio $v_s/v$ is less than 0.17, as shown in Fig. 16b. The viscosity ratio $v_s/v$ also varies in time and space in an intermittent

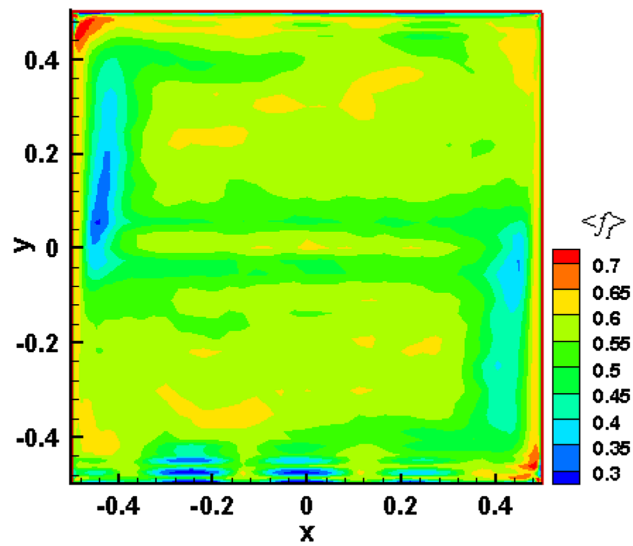


**Fig. 17** Contours of the *t-z* averaged FSI in the square section

behavior, it must be zero in some local regions where the instantaneous swirling strength vanishes.

To see the intermittence more clearly, the contours of the *t-z* averaged FSI denoted by $< f_I >$ in the square section are illustrated in Fig. 17. Impacted by the loop wall jet and wall temperatures, the heterogeneity of the averaged FSI in the near wall region becomes more evident, but in the core region, it decreases and tends to become relatively homogeneous. The averaged FSI in the left-top and right-bottom corner regions can arrive at a value over 0.65, but there are two accompanying regions where the averaged FSI is less than 0.4.

## 5 Conclusions

A LES was conducted to explore the turbulent air natural-convection in a differentially heated square cavity at a Rayleigh number of $5.33 \times 10^9$. By virtue of a finite

**Fig. 16** Iso-surfaces of FSI (**a**) and viscosity ratio (**b**) in the 1/8 domain of simulation. Note that the iso-surfaces of FSI in part **a** are labeled by 0.83, with the iso-surfaces of viscosity ratio in part **b** labeled by 0.17

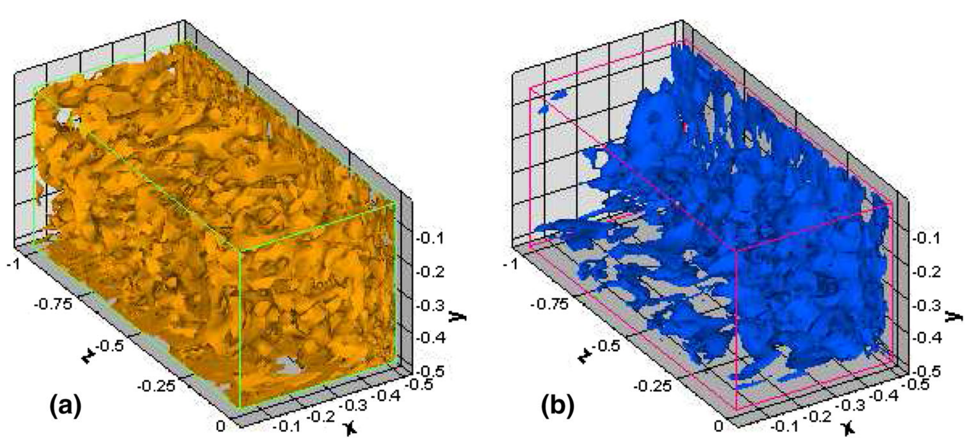

difference method, the LES reveals that the mean profiles, the rms values of velocities and temperature, and the Nusselt numbers agree well with the existing numerical and experimental data, suggesting that the relevant swirling strength based SGS model is of potential. By demonstrating the spontaneous iso-surfaces of FSI and viscosity ratio, it was found that the natural-convection is certainly intermittent. Affected by the loop wall jet and the assigned temperature on the horizontal walls, the *t-z* averaged FSI distribution in the square section shows that the heterogeneity of the averaged FSI in the near wall region is more evident, but in the core region of the square cavity, this heterogeneity decreases and the air natural-convection tends to become relatively homogeneous. Depending on the cavity geometry, the present LES indicates that the air natural-convection at Rayleigh number $5.33 \times 10^9$ certainly has its own characteristics in turbulence intermittency.

**Acknowledgments** This work is supported by NSFC(11372303). We are grateful to Dr J.L. Niu in the Hong Kong Polytechnic University and Dr N.N. Smirnov in Moscow State University for some private communications. We thank the anonymous referees for their invaluable suggestions.

## Appendix

Numerical test of sub-grid viscosity

To compare the present SGS model with that previously proposed by Vreman [54], we select a three-dimensional flow field based on the analysis of thermal instability of a layer of fluid heated from below with the effect of rotation [49], the steady flow field is given by:

$$\begin{cases} v_1 = -\frac{\pi}{a^2}\left[a_x \sin(a_x x)\cos(a_y y) + \frac{\sqrt{T}}{\pi^2 + a^2} a_y \cos(a_x x)\sin(a_y y)\right] W_0 \cos(\pi z) \\ v_2 = -\frac{\pi}{a^2}\left[a_y \cos(a_x x)\sin(a_y y) - \frac{\sqrt{T}}{\pi^2 + a^2} a_x \sin(a_x x)\cos(a_y y)\right] W_0 \cos(\pi z) \\ v_3 = W_0 \cos(a_x x)\cos(a_y y)\sin(\pi z) \end{cases} \tag{22}$$

In the numerical test, we simply set $a_x = a_y = a/\sqrt{2}$, $a = \pi$, $W_0 = 1$, and the Taylor number $T = \frac{4\Omega^2}{v} d^4 = 1 \times 10^6$, where $\Omega$ is the angular speed of rotation around the *z*-axis, *d* is the depth of the fluid layer, *v* is the fluid kinematic viscosity. The domain is given by $\{x \in (0, 2\sqrt{2}), y \in (0, 2\sqrt{2}), z \in (-1, 1)\}$, it is partitioned by $51 \times 51 \times 51$ grids. The grids are distributed uniformly in each direction. The calculated contours of the sub-grid viscosity are shown in Fig. 1a–b, evidently the viscosity distributions are different.

## References

1. Holmes P, Lumley JL, Berkooz G (1996) Turbulence, coherent structures, dynamicsal systems and symmetry. Cambridge University Press, Cambridge
2. Betelin VB, Smirnov NN, Nikitin VF, Dushin VR, Kushnirenko AG, Nerchenko VA (2012) Evaporation and ignition of droplets in combustion chambers modeling and simulation. Acta Astronautica 70:23–35
3. Corvaro F, Paroncini M (2009) An experimental study of natural convection in a differentially heated cavity through a 2D-PIV system. Int J Heat Mass Transf 52:355–365
4. Salat J, Xin S, Joubert P, Sergent A, Penot F, Le Quéré P (2004) Experimental and numerical investigation of turbulent natural convection in a large air-filled cavity. Int J Heat Fluid Flow 25:824–832
5. Tian YS, Karayiannis TG (2000) Low turbulence natural-convection in an air filled square cavity part I: the thermal and fluid flow fields. Int J Heat Mass Transf 43:849–866
6. Tian YS, Karayiannis TG (2000) Low turbulence natural-convection in an air filled square cavity part II: the turbulence quantities. Int J Heat Mass Transf 43:867–884
7. Saury D, Rouger N, Djanna F, Penot F (2011) Natural convection in an air-filled cavity: experimental results at large Rayleigh numbers. Int Commun Heat Mass Transf 38:679–687
8. Ishida H, Kawase S, Kimoto H (2006) The second largest Lyapunov exponent and transition to chaos of natural-convection in a rectangular cavity. Int J Heat Mass Transf 49:5035–5048
9. Sathiyamoorthy M, Basak T, Roy S, Pop I (2007) Steady natural convection flows in a square cavity with linearly heated side wall (s). Int J Heat Mass Transf 50:766–775
10. Bilgen E, Ben Yedder R (2007) Natural-convection in enclosure with heating and cooling by sinusoidal temperature profiles on one side. Int J Heat Mass Transf 50:139–150
11. Basak T, Roy S, Balakrishnan AR (2006) Effects of thermal boundary conditions on natural-convection flows within a square cavity. Int J Heat Mass Transf 49:4525–4535
12. Kao PH, Chen YH, Yang RJ (2008) Simulations of the macroscopic and mesoscopic natural-convection flows within rectangular cavities. Int J Heat Mass Transf 51:3776–3793
13. Mondal B, Li XG (2010) Effect of volumetric radiation on natural convection in a square cavity using lattice Boltzmann

method with non-uniform lattices. Int J Heat Mass Transf 53:4935–4948
14. Aounallah M, Addad Y, Benhamadouche S, Imine O, Adjlout L, Laurence D (2007) Numerical investigation of turbulent natural-convection in an inclined square cavity with a hot wavy wall. Int J Heat Mass Transf 50:1683–1693
15. Sharma AK, Velusamy K, Balaji C (2008) Interaction of turbulent natural convection and surface thermal radiation in inclined square enclosures. Heat Mass Transf 44:1153–1170
16. Niu JL, Zhu ZJ (2004) Numerical evaluation of weakly turbulent flow patterns of natural-convection in a square enclosure with differentially heated sideWalls. Numer Heat Transfer Part A 45(6):551–568
17. Hanjalic K (2002) One-point closure model for buoyancy-driven turbulent flows. Ann Rev Fluid Mech 34:321–347
18. Ma LD, Li ZY, Tao WQ (2007) Direct numerical simulation of turbulent flow and heat transfer in a square duct with natural convection. Heat Mass Transf 44(2):229–250
19. Manhart M (2004) A zonal grid algorithm for DNS of turbulent boundary layers. Comput Fluids 33:435–461
20. Groetzbach G (1982) Direct numerical simulation of laminar and turbulent Benard convection. J Fluid Mech 119:27–53
21. Trias FX, Soria M, Oliva A, Pérez-segarra CD (2007) Direct numerical simulations of two- and three-dimensional turbulent natural convection flows in a differentially heated cavity of aspect ratio 4. J Fluid Mech 586:259–293
22. Trias FX, Gorobets A, Soria M, Oliva A (2010) Direct numerical simulation of a differentially heated cavity of aspect ratio 4 with Rayleigh numbers up to $10^1 1$ C part I: numerical methods and time-averaged flow. Int J Heat Mass Transf 53:665–673
23. Trias FX, Gorobets A, Soria M, Oliva A (2010) Direct numerical simulation of a differentially heated cavity of aspect ratio 4 with Rayleigh numbers up to $10^1 1$ C part II: heat transfer and flow dynamics. Int J Heat Mass Transf 53:674–683
24. Friedrich R, Su MD (1982) Large eddy simulation of a turbulent wall-bounded shear layer with longitudinal curvature. Lecture Notes Phys 170:196–202
25. McMillan OJ, Ferziger JH (1979) Direct testing of sub-grid-scale models. AIAA J 17(12):1340–1346
26. Peng SH, Davidson L (2002) On a sub-grid scale heat flux model for large eddy simulation of turbulent thermal flow. Int J Heat Mass Transf 45:1393–1405
27. Peng SH, Davidson L (2001) Large eddy simulation for turbulent buoyant flow in a confined cavity. Int J Heat Fluid Flow 22:323–331
28. Smagorinsky JS (1963) General circulation experiments with the primitive equations, the basic experiment. Mon Wea Rev 91(3):99–164
29. Moin P, Kim J (1982) Numerical investigation of turbulent channel flow. J Fluid Mech 118:341–377
30. Madabhushi RK, Vanka SP (1991) Large eddy simulation of turbulence-driven secondary flow in a square duct. Phys Fluids A 3(11):2734–2745
31. Su MD, Friedrich R (1994) Investigation of fully developed turbulent flow in a straight duct with large eddy simulation. ASME J Fluid Eng 116(4):677–684
32. Vázquez MS, Métais O (2002) Large-eddy simulation of the turbulent flow through a heated square duct. J Fluid Mech 453:201–238
33. Métais O, Lesieur M (1996) New trend in large eddy simulation of turbulence. Annu Rev Fluid Mech 28:45–82
34. Pallares J, Davidson L (2000) Large-eddy simulations of turbulent flow in a rotating square duct. Phys Fluids 12:2878–2894
35. Pallares J, Davidson L (2002) Large-eddy simulations of turbulent heat transfer in stationary and rotating square ducts. Phys Fluids 14:2804–2816
36. Cui GX, Zhou HB, Zhang ZS, Shao L (2004) A new subgrid eddy viscosity model and its application. Chin J Comput Phys 21(3):289–293 (in Chinese)
37. Cui GX, Xu CX, Zhang ZS (2004) Progress in large eddy simulation of turbulent flows. Acta Aerodyn Sinica 22(2):121–129 (in Chinese)
38. Li JC (2001) Large Eddy simulation of complex turbulent flows: physical aspects and research trends. Acta Mech Sinica 17(4):289–301
39. Sergent A, Joubert P, Le Quéré P (2003) Development of a local sub-grid diffusivity model for large-eddy simulation of buoyancydriven flows: application to a square differentially heated cavity. Numer Heat Transf Part A 44:789–810
40. Sagaut P, Troff B, Le TH, Ta Phuoc Loc (1996) Large eddy simulation of flow past a backward facing step with a new mixed scales SGS model. In: IMACS-COST conference on computation of three-dimensional complex flows. Notes Numer Flow Dyn 53:271–278
41. Barhaghi DG, Davidson L (2007) Natural convection boundary layer in a 5:1 cavity. Phys Fluids 19:125106
42. Holm DD (1999) Fluctuation effects on 3D Lagrangian mean and Eulerian mean fluid motion. Phys D 133(1–4):215–269
43. Cheskidov A, Holm DD, Olson E, Titi ES (2005) On a Leray-α model of turbulence. Proc R Soc Lond A 461(2055):629–649
44. Geurts BJ, Holm DD (2003) Regularization modeling for large-eddy simulation. Phys Fluids 15(1):L13CL16
45. van Reeuwijk M, Jonker HJJ, Hanjalic K (2008) Wind and boundary layers in RayleighCBnard convection. I. Analysis and modelling. Phys Rev E 77:036311
46. van Reeuwijk M, Jonker HJJ, Hanjalic K (2009) Leray-α simulations of wall-bounded turbulent flows. Int J Heat Fluid Flow 30:1044–1053
47. Trias FX, Verstappen RWCP, Gorobets A, Soria M, Oliva A (2010) Parameter-free symmetry-preserving regularization modeling of a turbulent differentially heated cavity. Comput Fluids 39:1815–1831
48. Verstappen R (2008) On restraining the production of small scales of motion in a turbulent channel flow. Comput Fluids 37:887–897
49. Chandrasekhar S (1961) Hydrodynamic and hydromagnetic stability. Chap III. Oxford University Press, Cambridge
50. Zhu ZJ, Niu JL, Li YL (2014) Swirling-strength based large eddy simulation of turbulent flows around a single square cylinder at low Reynolds numbers. Appl Math Mech Eng
51. Zhou J, Adrian RJ, Balachandar S, Kendall TM (1999) Mechanisms of generating coherent packets of hairpin vortices in channel flow. J Fluid Mech 387:353–396
52. Ganapathisubramani B, Longmire EK, Marusic I (2006) Experimental investigation of vortex properties in a turbulent boundary layer. Phys Fluids 18:155105
53. Lin CT, Zhu ZJ (2010) Direct numerical simulation of incompressible flows in a zero-pressure gradient turbulent boundary layer. Adv Appl Math Mech 2(4):503–517
54. Vreman AW (2004) An eddy-viscosity sub-grid-scale model for turbulent shear flow: algebraic theory and applications. Phys Fluids 16(10):3670–3681
55. Wakitani S (2001) Numerical study of three dimensional oscillatory natural-convection at low Prandtl number in rectangular enclosures. ASME J Heat Transf 123:77–83
56. Yang HX, Chen TY, Zhu ZJ (2009) Numerical study of forced turbulent heat convection in a straight square duct. Int J Heat Mass Transf 52(13–14):3128–3136

57. Zhu ZJ, Yang HX, Chen TY (2010) Numerical study of turbulent heat and fluid flow in a straight square duct at higher Reynolds numbers. Int J Heat Mass Transf 53:356–364
58. Harlow FH, Welch JE (1965) Numerical calculation of time dependent viscous incompressible flow of fluid with free surface. Phys Fluids 8:2182–2196
59. Nikitin N (2006) Finite-difference method for incompressible Navier-Stokes equations in arbitrary orthogonal curvilinear coordinates. J Comput Phys 217:759–781
60. Papanicolaou E, Jaluria Y (1992) Transition to a periodic regime in mixed convection in a square cavity. J Fluid Mech 239:489–509
61. Khanafer K, Vafai K, Lightstone M (2002) Mixed convection heat transfer in two dimensional open-ended enclosures. Int J Heat Mass Transf 45(26):5171–5190
62. Trias FX, Gorobets A, Oliva A (2013) A simple approach ro discretize the viscous terms with spatially varying (eddy-) viscosity. J Comput Phys 253:405–417
63. Brown DL, Cortez R, Minion ML (2001) Accurate projection methods for the incompressible Navier-Stokes equations. J Comput Phys 168:464–499
64. Yang HX, Zhu ZJ (2004) Exploring super-critical properties of secondary flows of natural-convection in inclined channels. Int J Heat Mass Transf 47:1217–1226
65. Baker TJ (1981) Potential flow calculation by the approximate factorization method. J Comput Phys 42:1–19
66. Zhu ZJ, Yang HX (2003) Numerical investigation of transient laminar natural-convection of air in a tall cavity. Heat Mass Transf 39:579–587
67. Fusegi T, Hyun JM, Kuwahara K (1991) Transient three-dimensional natural convection in a differentially heated cubical enclosure. Int J Heat Mass Transf 34:1559–1564